PROCEEDINGS OF SPIE

SPIEDigitalLibrary.org/conference-proceedings-of-spie

A novel surface plasmon coupled tunable wavelength filter for hyperspectral imaging

John F. Turner, Ajaykumar H. Zalavadia

SPIE.

A novel surface plasmon coupled tunable wavelength filter for hyperspectral imaging

John F. Turner II and Ajaykumar H. Zalavadia
Cleveland State University, Department of Chemistry, Cleveland OH 44134, USA

ABSTRACT

The development of ultra-compact handheld hyperspectral imagers has been impeded by the scarcity of small widefield tunable wavelength filters. The widefield modality is preferred for handheld imaging applications in which image registration can be performed to counter scene shift caused by irregular user motions that would thwart scanning approaches. Conventional widefield tunable filters like the liquid crystal tunable filter and acousto-optic tunable filter achieve narrow passbands across a wide spectral range by utilizing large interaction lengths, thereby increasing the thickness of the device along the optical path. In addition, these technologies rely on rather bulky external control circuitry and, in the case of acousto-optic filters, high power requirements. In the work presented here, we introduce a novel widefield tunable filter for visible and near infrared imaging based on surface plasmon coupling that can be miniaturized without sacrificing performance. The surface plasmon coupled tunable filter (SPCTF) provides diffraction limited spatial resolution with a <10nm nominal passband and a spurious free spectral range of more than 300nm. Acting on the π-polarized component, the device is limited to transmitting 50 percent of unpolarized incident light. This is higher than the throughput of comparable Lyot-based liquid crystal tunable filters that employ a series of linear polarizers. The design of the SPTF is presented along with a comparison of its performance to calculated estimates of transmittance, spectral resolution, and spectral range.

Keywords: surface plasmon, tunable wavelength filters, hyperspectral imaging, surface plasmon resonance

1. INTRODUCTION

Hyperspectral imaging (HSI) is a set of techniques that has contributed to the study of advanced materials, pharmaceuticals, semiconductors, ceramics, polymers, biological specimens, and geological samples.[1-7] Its use for remote sensing has advanced our understanding of agriculture, forestry, the Earth, environmental science, and the universe.[5,7] By integrating wavelength selection devices with imaging optics and sensitive detectors, HSI enables spectral information from each assigned pixel location on a sample or target location to be recorded. Hyperspectral imagers have been developed for every optical region of the electromagnetic spectrum to measure variations in the absorption, emission, transmittance, reflectance, and scattering of light by complex samples. To accommodate this broad range of modalities, HSI instruments are custom-designed for specific applications. The essential hardware, acquisition control software, and data processing strategies can differ markedly among HSI instruments. Likewise, the type of information desired from the sample governs which type of spectroscopy is utilized. Regardless of its implementation, HSI produces a set of spectra in which each spectrum corresponds to an assigned location on or in the sample. To visualize changes in the sample across its spatial extents, data processing is performed on the hyperspectral data so that a pseudocolor image map or volume view of the sample can be rendered. Color differences in the rendered result correspond to meaningful variations in the spectral characteristics of the sample. Depending on the type of data processing performed, the numerical scores upon which this color-contrast is based can be used to extract either qualitative or quantitative information, or both.

A necessary capability of HSI instruments is wavelength tuning. Early multispectral imagers often utilized a small number of fixed bandpass filters, mounted in a filter wheel, that could be individually introduced into the optical path of the imaging detector. The data, while limited in scope, was often sufficient enough to allow meaningful differences across the field of view to be revealed by performing simple calculations such as dividing the image acquired for one band by another. Global illumination of the sample, either by sunlight or the use of a diffuse source, simplified data acquisition by enabling concurrent capture of pixel locations across the widefield area in a single snapshot using detector

Novel Optical Systems Design and Optimization XX, edited by Arthur J. Davis, Cornelius F. Hahlweg, Joseph R. Mulley, Proc. of SPIE Vol. 10376, 103760A
 · doi: 10.1117/12.2274671

arrays. For these experiments, the image resolution was determined by the magnification, the wavelength of light, and the pixel geometry and pixel density of the detector array. Many applications in remote sensing and microscopy, even today, use multispectral imaging. It remains an attractive alternative to HSI due to its high image resolution, small acquisition times, comparatively straightforward data analyses, ease of data visualization, and lower cost. Even so, spectral imaging has advanced far beyond these early multispectral implementations and there are now many types of imaging approaches. For widefield HSI, electro-optic devices like the acousto-optic tunable filter (AOTF), Fabry-Perot tunable filter (FPTF), and liquid crystal tunable filter (LCTF) are frequently used to provide wavelength selection. A number of specialized filters like the resonance ionization imaging detector (RIID), hybrid holographic-liquid crystal filters, and photonic crystals are also used.[8-21] In addition, wavelength multiplexing has been performed in widefield applications using step-scan interferometers and radio frequency (RF) multiplexed AOTFs.[22,23] Comparatively simple instruments that utilize a series of angle tuned fixed filters are also available.[24] Each of these approaches has been utilized for the widefield modality because they provide sufficiently high spatial resolution, are electronically tunable, and can be implemented in a way that imparts suitably small spatial aberrations.

Apart from the widefield modality, point-mapping and line scanning approaches that use optic fiber-coupled spectrographs equipped with sensitive multichannel detectors are also common.[25-29] An adaptation of line scanning, sometimes called pushbroom imaging, is useful in remote sensing applications in which the detector is moving relative to the target area. In scanning approaches, each frame of the array detector captures the wavelength-dispersed spectral information and the spatial map is built-up over time. To improve the signal-to-noise ratio in low-light applications, spatial multiplexing can be performed by introducing imaging optics and a spatial light modulator (SLM), such as a digital micromirror device (DMD), between the sample and the collection fiber. For binary encoding sequences in which each pixel either contributes fully or not at all to a measurement, Hadamard-based transformations are commonly used to recover the spectrum at each pixel in the image.[30,31] The benefits of scanning and spatial multiplexing approaches include high spectral resolution and large spectral range.

The work presented here introduces a novel widefield tunable filter for visible and near infrared HSI based on surface plasmon coupling. The surface plasmon coupled tunable filter (SPCTF) is designed to leverage advances in consumer-based technologies so that HSI can be incorporated into compact handheld devices. As already discussed, there are many types of HSI implementations. The complexities associated with these approaches have slowed the use of HSI beyond basic materials research, bioresearch, remote sensing, and military applications. Until recently, the high cost of sensitive array detectors, light sources (lasers), high performance imaging optics, and the need for specialized computer hardware for acquisition and data processing impeded the spread of HSI to the consumer marketplace. In the last decade, the use of large imaging arrays in consumer products like smart cell phones, aerial drones, self-driving vehicles, and powerful portable computers has become ubiquitous. The necessary components for high resolution imaging, including data storage and on-board graphical displays, are embedded into these devices along with wireless networking and file transfer capabilities. In addition, bright optical sources like solid-state lasers and broadband LEDs (light emitting diodes) are commonplace, affordable, and already exist in many of these products. The last impediments to consumer-based HSI by non-specialists are turnkey software applications for automated data processing and the availability of compact, inexpensive, high performance, and low power wavelength selection devices.

Our choice of which imaging strategy to use for compact, field-capable, HSI devices accounts for the capabilities and limitations of the potential modalities. Rapid data acquisition, high image resolution, narrow spectral resolution, broad spurious-free spectral range, and high signal-to-noise level are desirable. Unfortunately, there exists a tradeoff among the number of pixels imaged, the number of optical bands interrogated, the desired signal-to-noise level, and the total acquisition time.[32] Although a full consideration is beyond the scope of this work, some generalizations are useful to consider. For example, as the number of wavelengths increases, the widefield acquisition time increases, but the time for the scanning methods remains unchanged. Conversely, as the number of scanned pixel elements increases, there is no change in the duration of the widefield experiment, but longer acquisition times are needed for the scanning modalities. Data sparsity, a term used to describe that portion of the data that yields no relevant information, often leads to unnecessarily long acquisition times. For spatially complex samples, which are commonly studied using HSI, sparsity in the wavelength dimension is often greater than in the spatial dimensions, thereby making the widefield implementation more attractive. It is also important to consider the optical characteristics of the sample. For instance, longer exposure times are required to reach the desired signal-to-noise level in light-sensitive applications in which optical attenuation is applied to avoid sample damage. If a scanning modality is used in this circumstance, longer dwell times at each pixel

location are needed and the overall acquisition time increases. Conversely, little or no attenuation of the light may be needed for the widefield approach if the same radiant source is used because the light will be defocused, thereby resulting in less optical power per pixel at the sample. Hence the disparity between the scanning and widefield acquisition times diminishes when the total number of scanned steps approaches the number of optical bands for these types of samples.

The SPCTF was designed to exploit existing and forthcoming technologies to achieve useful HSI capability. The large detector arrays and embedded circuitry of existing consumer products are most easily adapted for the widefield imaging modality in which no mechanized or tightly-regimented scanning protocols are needed. Software modification of existing platforms can readily provide image postprocessing to account for image registration errors that might result from detector or sample motion during the acquisition period. In fact, many consumer cameras already make use of image registration algorithms, but do so to provide image stabilization during video recording or for reducing image blur in still pictures. Recent advances in computational imaging that enable post-acquisition refocusing of the image[33] will likely benefit widefield HSI approaches by allowing the user to retroactively confine the depth of field to within the sampled region so that off-sample regions in the image are ignored. Because the SPCTF preserves the trajectory of light rays in the Fourier space that lie within its acceptance angle, it can be easily integrated with computational imaging detectors.

As part of this work, we describe the design and construction of the SPCTF and give a theoretical description of surface plasmon generation in thin metal films. Experimental transmittance data as a function of wavelength and incident angle with respect to the metal film, deposited on a glass prism in the Kretschmann-Raether configuration, is presented along with theoretical estimates for comparison. We demonstrate wavelength tuning using a coupled surface plasmon interaction in a symmetric cavity created by closely juxtaposing two prisms with their coated hypotenuses facing each other. Using this configuration as the basis of the SPCTF design, we demonstrate HSI using the SPCTF for the first time and give the transmittance and bandpass values as a function of wavelength. By exploiting the sensitivity of surface plasmon generation to the angle of incident light, a narrow passband SPCTF is presented. The bandpass and acceptance angle of the narrow passband device are given along with a brief discussion of the relationship between short-range and long-range surface plasmons in the SPCTF.

2. THEORY

Plasma oscillations are cooperative oscillations of free electrons such as those that can be induced in metals. The quasi-particle representation of the collective oscillation frequency is called a plasmon. Surface plasmons are said to exist when the oscillations are mostly localized at the surface, usually at the interface of a thin metal film with a dielectric. Other types of interfaces, such as those that form at dielectric-dielectrics and dielectric-semiconductor boundaries can also support surface plasmons. The plasma waves are confined to the interface and exist as transverse magnetic (TM) waves that travel along the interface. At planar interfaces, the combined effect of the electron motion with the electromagnetic fields it creates in and around the metal are referred to as a surface plasmon polariton (SPP). While a full description of SPP generation is given by electromagnetic field theory, a classical treatment is useful for describing those aspects that involve reflection, transmission, and absorption of optical energy.

2.1 Optical excitation of surface plasmon polaritons

In optical refraction, which is described by Snell's Law and the Fresnel equations, the refractive index, $n = c_o/c_m$, is used to relate the velocity of light, c_o, in a vacuum to the wave velocity in a refractive medium, c_m. In non-optical substrates such as in metals, the behavior of electromagnetic radiation is described by Maxwell's equations which depend on the electric permittivity, ε, and magnetic permeability, μ. Because of dispersion, the refractive index, permittivity, and permeability are frequency dependent. It is convenient to recast the permeability and permittivity values for a substrate relative to their vacuum values so that $\varepsilon_r(\omega) = \varepsilon(\omega)/\varepsilon_o$ and $\mu_r(\omega) = \mu(\omega)/\mu_o$, where ω is the angular frequency and ε_r and μ_r are the relative permittivity and relative permeability, respectively. Maxwell's equations are generalized expressions that apply to optical refraction as well. The relationship between the n, ε_r, and μ_r is given by $n = \sqrt{\varepsilon_r \mu_r}$. Because most refractive substrates are non-magnetic at optical frequencies where $\mu_r \approx 1$, the refractive index can be approximated by letting $n \approx \sqrt{\varepsilon_r}$. In metals where damping occurs, the complex permittivity, $\bar{\varepsilon_r} = \varepsilon_r + i\varepsilon_r'$, is used

where ε_r' is the imaginary part of the permittivity. Hence, there exists a complex refractive index, $\bar{\varepsilon_r}$, with real, n, and imaginary, κ, parts such that $\bar{\varepsilon_r} = n^2 = (n + i\kappa)^2$.

Light incident on a metal film interacts with the electrons in the film that move in a manner to compensate for the incident field gradients. This motion accounts for the reflection of light by highly conductive metals. The extent to which electrons compensate for the applied field oscillations can be understood by considering the plasma frequency of the metal. When electrons are displaced by a small amount from their ions, a Coulombic restoring force results. The plasma frequency, ω_p, of a metal is the natural frequency at which the electrons collectively oscillate upon removal of the applied field. The magnitude of the Coulomb force governs the value of ω_p. At low field frequencies, the electrons can move in way that prevents the electric field from entering the metal. When the applied frequency exceeds ω_p, the field oscillations are too fast for the electrons to follow. Consequently, the metal can no longer reflect the light and the field propagates into the metal.

The momentum of optical photons at a given frequency is much smaller that the momentum associated with electron oscillations in most metals at the same frequency. This momentum mismatch makes it impossible to directly excite SPPs on a metal surface using light traveling in air. By exploiting the geometric arrangement between the incident ray and the metal surface in an optically refractive material, and by relying on damping in the metal, plasmonic motion can be induced on a metal surface by the incident ray. Two common geometric arrangements, the Kretschmann-Raether and Otto configurations, enable coupling of SPPs to incident photons (Figure 1). In both cases π-polarized light traveling in a right-angle prism is incident to the prism hypotenuse at an angle above the critical angle. In the Kretschmann-Raether configuration, which is used here to construct the SPCTF, the hypotenuse surface is coated in a thin metal film (~48nm Ag). For optical refraction in transparent materials, dispersion describes the change in refractive index as a function of the applied optical frequency. In the more complex case of a coupled interaction between photons and plasmons, dispersion can be thought of as the relationship between the applied optical frequency and the angular wavenumber, $k_x = 2\pi/\Lambda_x$. Here, Λ_x is the wavelength associated with the collective electron oscillation in the metal. The wavevector, $\boldsymbol{k}_x$, lies within the plane of incidence along the metal-dielectric (air) interface.

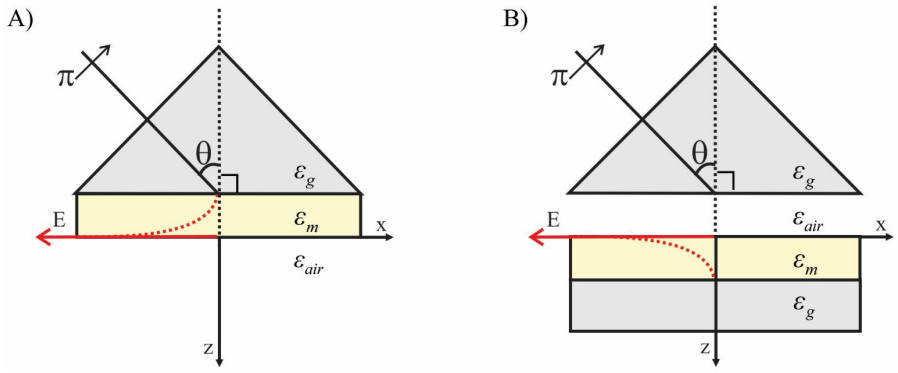

Figure 1. Optical excitation of SPPs. A) Kretschmann-Raether configuration. B) Otto configuration. The electromagnetic field associated with incident π-polarized light is converted to electron density fluctuations (surface plasmons) at the metal-dielectric interface corresponding to the boundary between ε_m and ε_{air}. The field amplitude is damped in the metal as a function of the z-axis position (red dotted line).

A plot of the dispersion curve as a function of angular wavenumber along the metal film, k_x, is shown in Figure 2. In air, the angular frequency of light, ω_{air}, exceeds the plasmon frequency except where k_x approaches zero. In refractive materials such as glass, the slope of the light line changes by $1/n$, enabling the light line to intersect the dispersion curve for electron motion at a suitably large k_x value. For the ω and k_x values at the intersection, coupling between photons and SPPs is possible for π-polarized light. Even though the incident angle at the prism hypotenuse exceeds the critical angle, θ_c, the reflected intensity approaches zero at the angle of surface plasmon resonance, θ_{sp}, which is dependent on the wavelength of light (λ), metal film thickness, and the dielectric properties of the metal and glass. While the surface plasmon dip is broad as a function of wavelength, SPPs occurs over a narrow range of incident angles and a sharp minimum is observed in the reflectivity as a function of incident angle at the hypotenuse. As the film thickness increases,

the efficiency of SPP coupling diminished due to the additional damping experienced by the electromagnetic fields during tunneling.

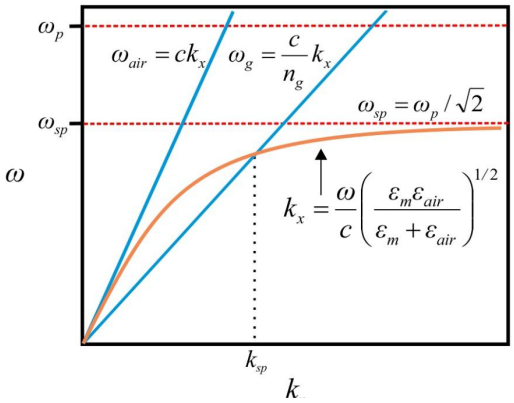

Figure 2. Dispersion at the metal-air interface of a metal-coated glass prism. Surface plasmons are generated at k_{sp} which corresponds to the point where the dispersion curve in the metal (orange) intersects with the light line in glass, ω_g. The light line in air, ω_{air} is shown for comparison.

In metals, the permittivity has real and imaginary parts. The imaginary part is related to damping and determines the frequency bandwidth over which SPP generation is possible. In addition, damping limits the propagation distance of SPPs along the metal surface and is responsible for short-range surface plasmon polariton (SRSPPs). For efficient SPP generation, the real part of the permittivity should be negative and larger in absolute magnitude than that of the dielectric. Gold and silver meet these requirements and are relatively easy to deposit on glass as thin films, but silver provides more efficient SPP coupling in the visible region. A published table of permittivity values for silver was used to estimate the real and imaginary permittivity values between 400nm and 900nm as shown in Figure 3.[34]

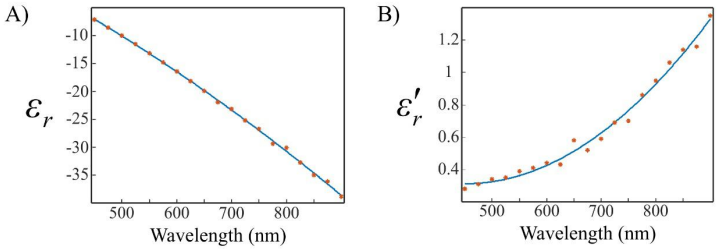

Figure 3. Complex permittivity of Ag. A) The real and B) imaginary parts of the relative permittivity as a function of wavelength. A second order polynomial (blue) was used to fit the data.

2.2 Theoretical calculation of reflectance loss by photon-polariton coupling

For a metal-coated prism in the Kretschmann-Raether configuration, the reflectance of light at the glass-metal interface will be attenuated by the generation of SPPs at the metal-air interface. Given the permittivities of the glass and metal film, Fresnel's equations can be used to calculate the reflectance at specified angle of incidence. A drop in the reflectance at angles greater than the critical angle are attributed to the conversion of photon energy in surface plasmon formation. A summary of the equations that result from the Fresnel approach are included here. The variable assignments are described in Figure 4 for the Kretschmann-Raether configuration employed in the construction of the SPCTF. The Fresnel expressions enable the calculation of the reflectance for the glass-metal and metal-air interfaces which are needed for elucidating the SPP conditions. The reflectance, R, is calculated from

$$R = |r_{ij}|^2 \ , \tag{1}$$

where r_{ij} is the reflection coefficient at the interface between the i^{th} and j^{th} substrates. For the glass-metal interface,

$$r_{gm} = \frac{\varepsilon_m k_{z_g} + \varepsilon_g k_{z_m}}{\varepsilon_m k_{z_g} - \varepsilon_g k_{z_m}} \ . \tag{2}$$

The magnitude of the wavevector component along the z-axis are given by k_{z_g} in the glass and k_{z_m} in the metal, where

$$k_{z_g} = \sqrt{\varepsilon_g {k_0}^2 - {k_x}^2} \tag{3}$$

and

$$k_{z_m} = \sqrt{\varepsilon_m {k_0}^2 - {k_x}^2} \ . \tag{4}$$

The magnitude of k_0 can be calculated from the vacuum wavelength, λ_0, according to $k_0 = 2\pi/\lambda_0$ and k_x, where

$$k_x = \eta_g k_o \sin\theta \ . \tag{5}$$

Because k_x is situated along the glass-metal interface and electromagnetic fields are continuous across the interface, the same k_x value is used for both z-axis components.

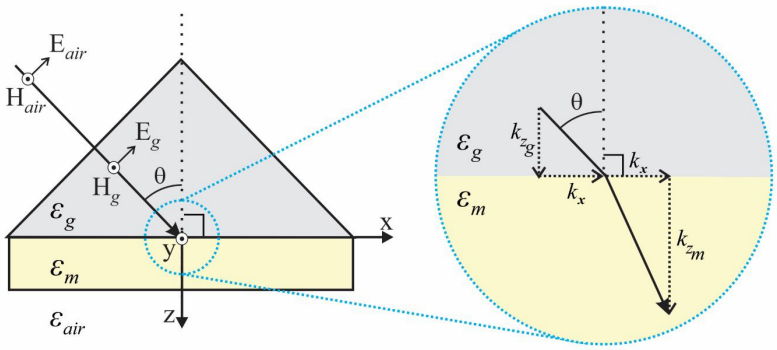

Figure 4. Variable assignments of the Kretschmann-Raether configuration for use in the Fresnel calculation of reflectance. Because the permittivity of air is close to the vacuum permittivity, $E_{air} \approx E_0$ and $\varepsilon_{air} \approx \varepsilon_0$.

This process is repeated for the metal-air interface in which the reflection coefficient is calculated from

$$r_{ma} = \frac{\varepsilon_a k_{z_m} + \varepsilon_m k_{z_a}}{\varepsilon_a k_{z_m} - \varepsilon_m k_{z_a}} \ , \tag{6}$$

where the permittivities, ε_a and ε_m, and z-axis components of the wavevectors in the metal, k_{z_m} (Eq. 4), and air, k_{z_a}, are used. Although not shown in Figure 4, the assignment of k_{z_a} is consistent with that for glass and metal, and its value can be calculated from

$$k_{z_a} = \sqrt{\varepsilon_a {k_o}^2 - {k_x}^2} \ . \tag{7}$$

For the multilayer glass-metal-air system, the complex amplitude of the π-polarized reflected light can be determined from Maxwell's equations by applying the condition of continuity to both interfaces. Upon simplification, the combined reflection coefficient, r_{gma} becomes

$$r_{gma} = \frac{r_{gm} + r_{ma}e^{i2dk_{z_m}}}{1 + r_{gm}r_{ma}e^{i2dk_{z_m}}} \tag{8}$$

and is dependent on the thickness, d, of the metal film.[35,36] The total reflectance of the glass-metal-air system can now be determined using the relation given in Eq. 1 so that

$$R = |r_{gma}|^2 = \left|\frac{r_{gm} + r_{ma}e^{i2dk_{z_m}}}{1 + r_{gm}r_{ma}e^{i2dk_{z_m}}}\right|^2 . \tag{9}$$

A minimum in the plot of reflectance as a function of incident angle, θ, represents the conversion of energy away from the reflected beam. When $\theta \geq \theta_c$, the energy loss is not accounted for in either the reflected or transmitted beams. Instead, the energy excites SPPs at the metal-air interface.

2.3 Surface plasmon coupling in a symmetrical resonant cavity

Optical characterization of metal-coated prims in the Kretschmann-Raether configuration is relatively straightforward as both the reflected and transmitted beams are readily accessible. Energy losses beyond those associated with non-ideal behavior of the substrates can be accounted for, to the extent that theory allows, by the formation of SPPs. While imperfect, there is substantial agreement between theory and empirical findings. The more challenging issues are related to understanding the SPP character, the behavior of electron groups as well as individual charges, and the way that surface non-uniformities in the metal and support substrate affect SPP propagation. The SPCTF described here is constructed from two prisms as described in Figure 5 that are closely juxtaposed with their metal-coated hypotenuses facing each other. In this arrangement, light incident on the first glass-metal interface can excite SPP at the metal-air interface. Due to the proximity of the second (identical) metal-coated prism, dipole-dipole coupling can drive SPP formation at its air-metal interface. Because both metal-coated prisms are identical, photon-plasmon coupling at the metal-air interface of the first prism can be expected to lead to plasmon-photon coupling at the air-metal interface of the second prism. As illustrated in the enlargement of Figure 4, the wavevector projection along the interface, k_x, is shared by both the incident and transmitted radiation such that $k_x = \eta_g k_o \sin\theta = 2\pi/\Lambda_x$. For coupling to occur, both frequency and momentum must be matched between the photon and plasmon. This occurs at θ_{sp} in the direction along k_x.

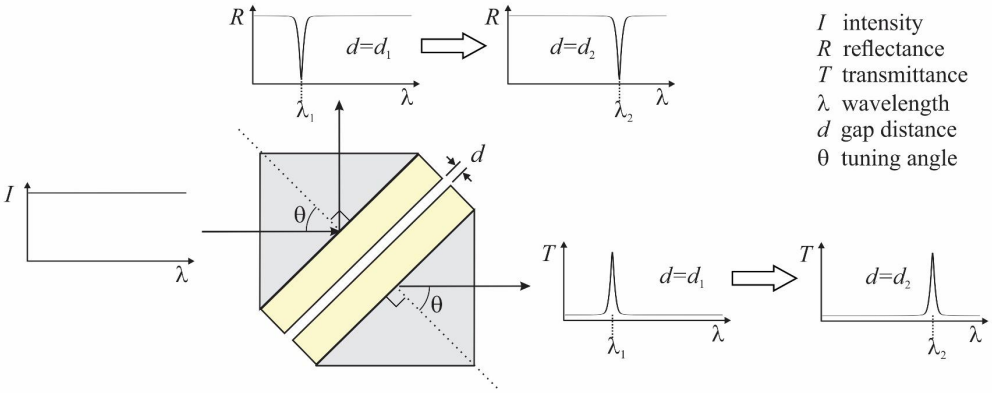

Figure 5. The SPCTF. Two metal coated prisms separated by a small tunable air-gap are used to provide wavelength tuning.

The SPCTF, which is constructed from two metal-coated prisms, can be loosely thought of as a merging of the Kretschmann-Raether and Otto configurations. The electromagnetic fields at the metal-air interfaces arising from electron motion as well as any evanescent contribution from the incident and coupled light fields are acted upon by the conditions of the resonant cavity as a whole. Hence, the extent of coupling of SPPs across the air gap is strongly dependent on the cavity geometry and dielectric properties. In addition, the phase relationship between plasmon oscillations in each metal influences the SPP coupling efficiency. The SPCTF exploits these properties to achieve

wavelength tuning of the coupled light by varying the gap distance. For uncollimated monochromatic light, a range of incident angles is presented to the SPCTF and more than one coupling mode can be populated simultaneously, depending on the gap distance. Due to free-electron scattering in the metal and surface roughness along the interfaces, SPPs localized to different regions on the metal films can experience different amounts of attenuation.[37] The attenuation range can span 100-fold or more, leading to a spread of SPP propagation distances. Therefore, only some of SPPs will meet the resonance conditions of the SPCTF cavity. Those SPPs which experience little attenuation exhibit greater propagation lengths and are known as long-range SPPs (LRSPPs). The short-range SPPs (SRSPPs) can be highly attenuated, thereby producing more localized effects across shorter distances.

3. EXPERIMENTAL

3.1 Sputter coating of Ag on BK-7 glass prisms

Thin Ag films were deposited using a 5.1cm diameter 13.56MHz magnetron sputter gun on the hypotenuses of BK-7 right angle prisms (Edmund Optics, 15mm) to a target thickness of 48nm. A modified sample mount was used that enabled a pair of prisms to be coated along with a polished piece of silicon without having to reopen the sputter chamber. The silicon substrates were used to experimentally validate film thickness using scanning electron microscopy (FEI, Inspect-F50). Sputtering was carried out in Ar gas at ~8mTorr pressure using an RF power of 60W. The background pressure with the Ar purge turned off and the pump throttle valve set partially closed, as it would be during deposition, was 2.2×10^{-5}Torr. A pressure of $\sim1\times10^{-6}$Torr was achieved with the pump throttle valve open. The sputter time was determined from earlier calibration trials in which Ag was sputtered on polished silicon substrates for a range of deposition times under the same experimental conditions that were used for the prisms. In addition, a quartz microbalance was used to monitor progress. Once coated, the prisms and samples were removed and immediately placed in a vessel under Ar purge that was then sealed.

3.2 Reflectance as a function of incident angle and wavelength

To determine the angle of incident illumination necessary for SPP formation, the coated prism was placed on the central stage of a pair of rotational stages that shared a common axis of rotation as shown in Figure 6. Independent rotation of each motorized stage (Cognisys, ROTO_TAB_01) was provided by a USB connected controller (Cognisys, STKS-C-3X) to achieve a step accuracy of 0.01^{o}. A 150W quartz tungsten halogen (QTH) lamp (GELCO FDS/DZE 24V) coupled to a 3mm diameter liquid light guide (Thorlabs, 2000 Series) was used to provided broadband illumination. Light exiting the light guide was collimated using an f/2 lens and then wavelength filtered to the desired range between 550nm and 850nm using a 550nm long-pass filter followed by an 850nm short-pass filter (Edmund Optics). Further collimation was achieved using series of 1mm apertures placed before and after a linear polarizer (Thorlabs, GTH10MA) that was oriented to provide π-polarized light at the prism hypotenuse. A slit placed immediately before the prism was used to further reduce beam spread in the plane of incidence. Light reflected from the prism hypotenuse was focused into a 200μm collection fiber (CeramOptec) using an f/2 lens (Edmund Optics). The lens and collection fiber were mounted on a rail extending out from the center of the second rotational stage to enable angular positioning. The distal end of the fiber was coupled to an imaging spectrograph (Chromex, 500IS/SM) equipped with a liquid nitrogen-cooled charge coupled device (CCD) detector (Roper/Princeton Instruments, EEV 400X1340B) for spectral acquisition. To ensure capture of the reflected light, a series of spectra were recorded for each 0.1^{o} increment of prism rotation by scanning the collection fiber by 0.05^{o} increments across the reflected beam. This approach also safeguarded against any mechanical play in the rotational stage assembly.

Data collection was automated using a Windows application written in Visual C++ that controlled the rotational stages as well as all aspects of CCD acquisition such as exposure time, chip-temperature ($-90C^{o}$), and file handling. Wavelength calibration was performed using a spectrum acquired from a neon lamp (Newport, 6032). To enable calculation of the SPCTF reflectance, the prism was removed and a spectrum of the illumination was recorded. A background spectrum, recorded by blocking the illumination, was subtracted from all spectra prior to taking the ratio of the reflected light spectra with respect to the illumination spectrum. Comparison of this data to theoretical estimates is performed by first adjusting the theoretical calculation to account for reflection losses at the entrance and exit faces of the BK-7 prims. All data processing was performed using code written in MatLab (The MathWorks).

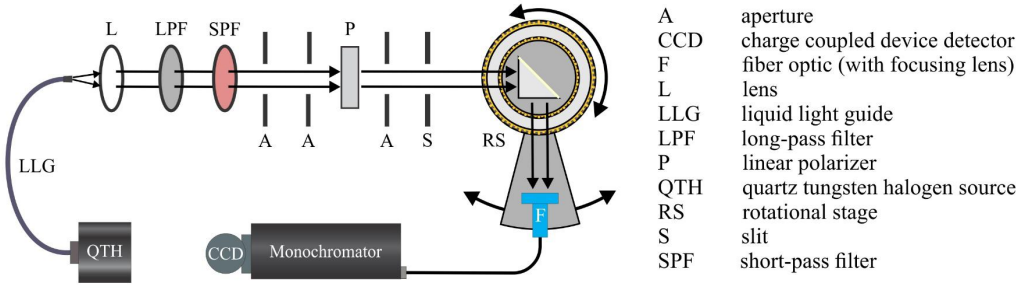

Figure 6. Schematic diagram of the optical setup for reflectance measurements

3.3 Reflectance of angularly dispersed light as a function of incident angle and wavelength

Because the formation of SPPs is very sensitive to the angle of incident light, the use of angularly dispersed light can significantly reduce the spectral bandwidth of light that can couple to SPPs. There are a number of applications that would benefit from the use of thin transmissive dispersers in combination with plasmonic devices to provide narrow passband tuning. To test the efficacy of this approach, the apparatus used to measure the reflectance of angularly dispersed light from the prism hypotenuse was adapted from the design shown in Figure 6. In the first of two modifications, a transmission grating (Thorlabs, GT25-06V) was placed in the optical path immediately before the prism. The angular change in the optic path caused by the diffraction grating necessitated the second modification, a repositioning of the dual stage and fiber collection optics as shown in Figure 7. Data collection was performed as described in section 3.2. Because the light is collected over a range of reflected angles for each orientation of the prism, and because each reflected angle corresponds to a different wavelength, most of which are not generating SPPs, it is not necessary to take a separate spectrum of the illumination in order to calculate the transmittance. Because the incident angles in the dispersed beam are above the critical angle, the set of maxima extracted from each spectrum acquired for one prism orientation, after subtracting the background spectrum, is an envelope function that matches the illumination spectrum except in the vicinity of the surface plasmon-coupled wavelengths. The neighboring sets of envelope spectra, acquired for other prism orientations that exhibit a wavelength shift in the SPP coupling, can be used to establish an intensity surface as a function of wavelength and prism orientation angle. Surface contours that neighbor the plasmon intensity dip in the surface can be used to make accurate estimates of the illumination intensity in the plasmon dip regions. This self-referenced approach avoids many of the experimental errors and alignment challenges related to removing the prism so that a properly scaled illumination spectrum can be acquired.

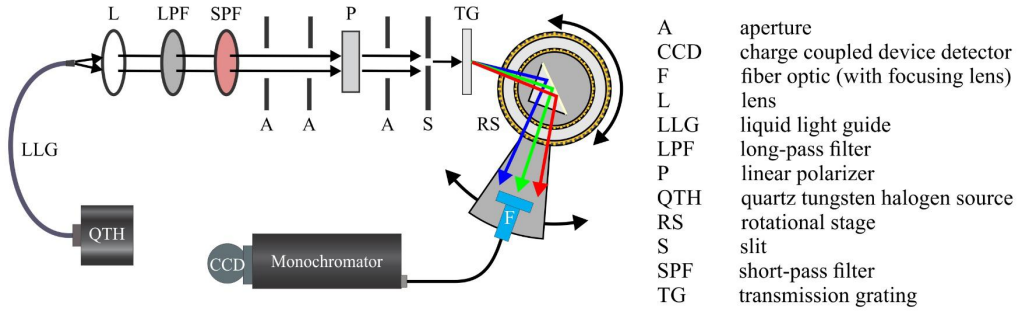

Figure 7. Schematic diagram of the optical setup for reflectance measurements of angularly dispersed light.

3.4 Construction and characterization of the SPCTF

The SPCTF was constructed by affixing both prims to aluminum rods using 330 epoxy (Hughes Associates). The rods were inserted into the channels of a custom aluminum enclosure that had openings to expose the optical surfaces of the SPCTF. One prism was held stationary while that other could be moved by turning a finely threaded screw, thereby

adjusting the air gap between the prisms. Assembly of the prism enclosure was performed prior to curing of the epoxy so that the prisms could be brought into contact with each other during the cure time to establish a sufficiently parallel alignment between their hypotenuses. Once construction of the SPCTF enclosure was complete, the assembly was mounted in place of the rotating stages and the fiber collection optics were repositioned as shown in Figure 8. A series of spectra were collected for a range of SPCTF gap distances along with a spectrum of the illumination that was acquired by removing the SPCTF. A background spectrum was subtracted from all spectra prior to taking the ratio of the transmitted light spectra with respect to the illumination spectrum.

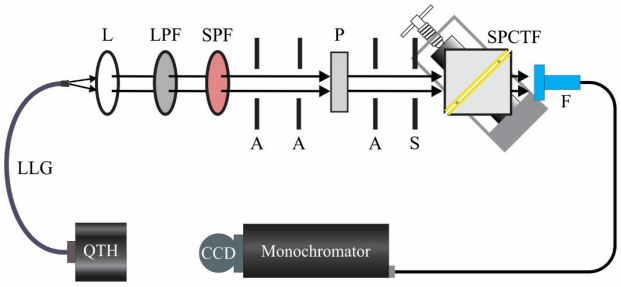

A	aperture
CCD	charge coupled device detector
F	fiber optic (with focusing lens)
L	lens
LLG	liquid light guide
LPF	long-pass filter
P	linear polarizer
QTH	quartz tungsten halogen source
S	slit
SPCTF	surface plasmon-coupled tunable filter
SPF	short-pass filter

Figure 8. Apparatus for measuring SPCTF transmittance.

The bandpass and acceptance angle of the SPCTF was determined for angularly dispersed light using the apparatus shown in Figure 9. A reflective grating (Thorlabs, 600g/mm) was placed in the optical path to provide angular dispersion. Although not shown, the grating was mounted on a rotational mount (Thorlabs, PR01) to enable wavelength tuning along the acceptance path of the SPCTF. Spectra of the transmitted light were acquired over a range of SPCTF angles for each of several gap distances using a rotational stage (Cognisys, ROTO_TAB_01). The collection fiber remained fixed in position.

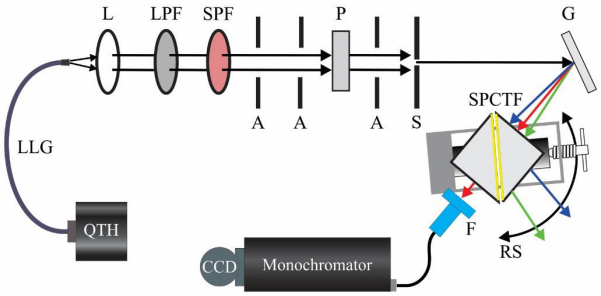

A	aperture
CCD	charge coupled device detector
F	fiber optic (with focusing lens)
G	grating
L	lens
LLG	liquid light guide
LPF	long-pass filter
P	linear polarizer
QTH	quartz tungsten halogen source
RS	rotational stage
S	slit
SPCTF	surface plasmon-coupled tunable filter
SPF	short-pass filter

Figure 9. Apparatus for measuring SPCTF transmittance of angularly dispersed light.

3.5 SPCTF hyperspectral imaging

The schematic diagram in the Figure 10 is an illustration of the optical setup used to perform proof-of-principle SPCTF hyperspectral imaging for the first time. The sample, a stained pine stem cross-section (Carolina Biology Supply Co.) mounted in glass, was chosen for its inherent color-contrast in the operating range of the SPCTF and its well-defined morphology. Illumination was performed in transmission mode using a broadband QTH source coupled to a refractive microscope (Olympus, BX-60). The transmitted light from the sample was collected using an infinity corrected 10× object (Olympus, 0.30 NA) and polarized using a Glan-Thompson prism (Thorlabs, GTH10MA) before wavelength filtering by the SPCTF. Image acquisition was performed using a liquid nitrogen-cooled CCD (Roper Scientific EEV1024x1024B) coupled to image reformation optics. A series of images between 450nm and 700nm were acquired at 25nm increments by adjusting the air gap of the SPCTF. The hyperspectral data were processed using spectral identity mapping (SIM) analysis to reveal wavelength-dependent differences across the field of view.[38]

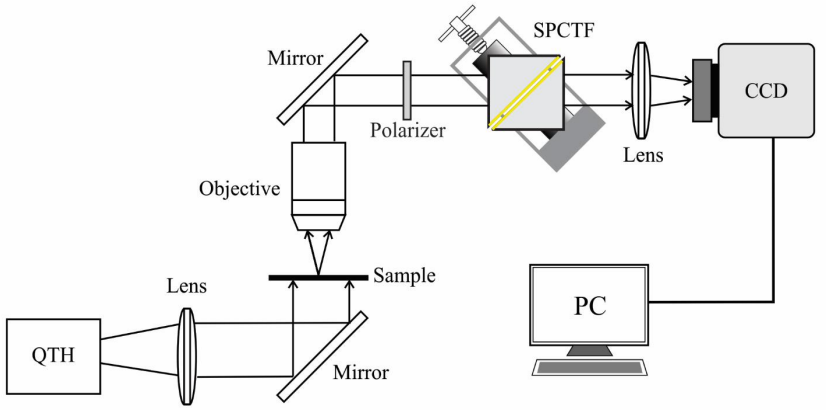

Figure 10. SPCTF hyperspectral imaging microscopy.

4. RESULTS

4.1 Reflectance from the glass-metal interface

The theoretical reflectance at the glass-metal interface, as calculated using Eq. 9, is shown as a function of illumination wavelength and incident angle at the glass-metal interface in Figure 11. There is an increase in the reflectance as the incident angle approaches the critical angle of ~42°. For larger incident angles in uncoated prisms, the reflectance is 1. For a coated (Kretschmann-Raether) prism, there is a sharp dip in the reflectance between 43° and 44° degrees that corresponds to SPP generation at the metal-air interface. As shown more clearly in Figure 11B, there is a wavelength dependence on the angle of maximal surface plasmon generation. The rough appearance at the base of the plasmon dip in Figure 11A is an artifact arising from the finite increments for wavelength and incident angle that were used to calculate the surface. A Fresnel correction was applied to account for losses due to reflections at the entrance and exit faces of the prism.

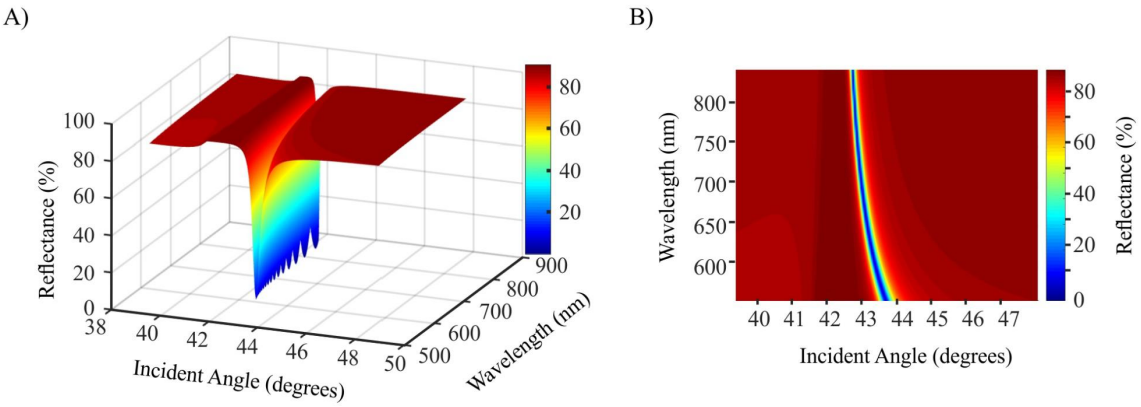

Figure 11. Theoretical reflectance from the glass-metal interface of a silver-coated prism in the Kretschmann-Raether configuration. A) The reflectance surface shows a sharp drop corresponding to the formation of SPPs at an angle greater than the critical angle. B) Viewed as an image, the wavelength dependence of the incident angle necessary for plasmon formation is apparent.

Using the experimental setup described in section 3.2, the reflected intensity from the glass-metal interface of a silver-coated prism was measured as function of wavelength and incident angle. The data results are shown in Figure 12 and are in qualitative agreement with the theoretical estimates (Figure 11) to within experimental error. For example, there is an increase in the reflected light as the incident angle approaches the expected critical angle of 42° and the angular

position of the surface plasmon dip, in the vicinity of 43°, exhibits the expected wavelength dependency. Because the silver was not protected from oxidation during data acquisition, significant attenuation of the SPP is expected. Due to the large amount of data necessary to generate the reflectance surface, a short exposure time (1s) was used to reduce the total acquisition time. While sufficient, the moderate signal-to-noise level is a consequence of the tradeoff between signal intensity and acquisition time. Traces from the reflectance surface for several angles of incidence and wavelength are shown in Figures 12C and 12D. The surface plasmon dip is broad in the wavelength dimension and nominally spans ~ 70nm. Conversely, the formation of SPPs is very sensitive to the angle of incidence, spanning less than 2° over the wavelength range from 550nm to 850nm as shown in Figure 12D. This angular sensitivity can be exploited to reduce the optical bandpass of the SPCTF as shown in section 4.5.

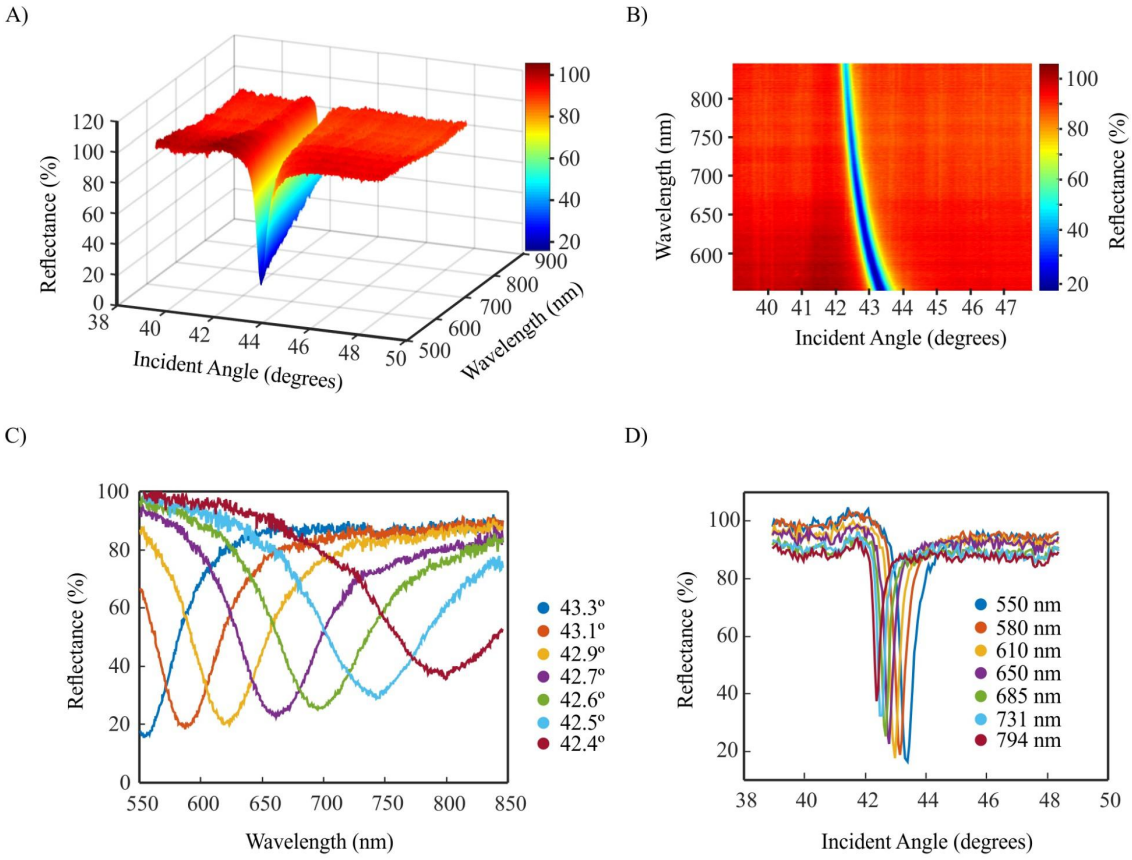

Figure 12. The reflected intensity from the glass-metal interface of a silver-coated prism as function of wavelength and incident angle. The reflectance surface and image, shown in A) and B) agree qualitatively with the theoretical estimates shown in Figure 11. Traces of the reflectance surface as a function of wavelength and incident angle are shown in C) and D). Although SPPs can couple over a large wavelength range, they are very dependent on the angle of illumination.

4.2 Reflectance of dispersed light from the glass-metal interface

Figure 13 shows a reflectance surface in which yellower regions exhibit higher reflectance values than bluer regions. The data was obtained using the method described in section 3.3 in which a grating is placed in the optical path before the prism. A comparison of the image in Figure 13 to the one shown in Figure 12B reveals that the use of a dispersive element in the optical path of the prism reduces the wavelength bandwidth over which photon-polariton coupling can occur. This data demonstrates that angular dispersion in conjunction with plasmonic excitation can be used to create a narrowband optical filter. A description of the potential impact of this illumination approach is given in section 4.5 for the SPCTF.

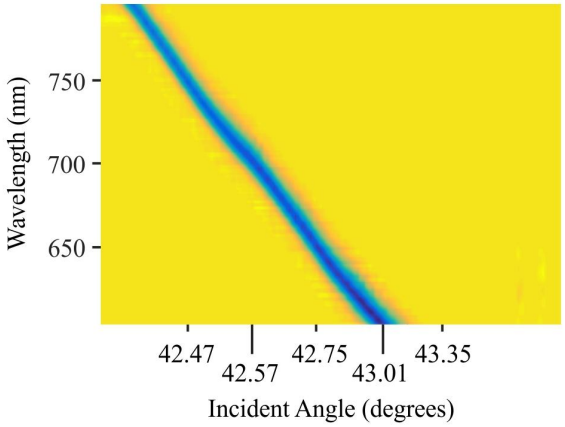

Figure 13. Reflectance image as a function of wavelength and incident angle using angularly dispersed illumination. The location of the surface plasmon dip is shown in blue while yellow regions indicate reflectance values that approach 1. The use of angularly dispersed light narrows the optical bandwidth over which photon-polariton coupling can occur.

4.3 SPCTF throughput and bandpass

For a single metal-air interface, different wavelengths couple at different incident angles. Wavelength tuning in the SPCTF, however, is accomplished for a fixed incident angle by changing the air gap distance between the two metal-air interfaces that comprise its resonant cavity. A series of SPCTF transmittance spectra are shown in Figure 14 for a progression of gap distances that increase for increasing passband wavelength. While the air gaps are nominally less than 1μm, the exact gap distance is not known. The measured bandwidths are likely larger than would be predicted for ideal substrates due to surface roughness in the glass and metal. In addition, no feedback mechanism was in place to either monitor or actively control the degree of parallelism of the metal-air interface during tuning. Hence the observed SPCTF transmittance (>25%) and bandpass values (~70nm, nominally) would likely improve by employing smaller and flatter substrates, and by replacing the mechanically-adjusted air gap with precision electro-optic tuning.

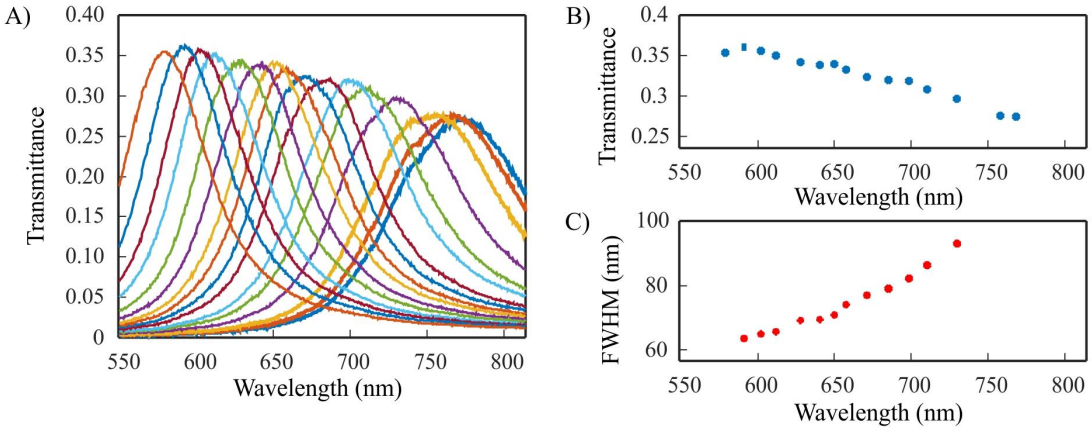

Figure 14. Wavelength tuning by the SPCTF. A) Transmittance spectra are shown for a series of air gap distances. At larger gap distances, the passband shifts to longer wavelengths. B) and C) The SPCTF transmittances and bandwidths (at FWHM) are shown as a function of passband wavelength.

4.4 Short-range and long-range surface plasmons

The distances over which SPPs propagate are dependent on the amount of attenuation. Free electron scattering in the metal and roughness at the interfaces are two important causes of SPP attenuation that can adversely affect the performance of plasmonic devices. While low attenuation leads to the sought-after LRSPPs, plasmonic devices often have imperfections that lead to the formation of both SRSPPs and LRSPPs. Because the SPCTF cavity is tunable, the LRSPPs can be preferentially selected over the SRSPPs by choosing the largest gap distance capable of generating SPPs at the desired wavelength. Figure 15A shows the SPCTF passband intensity for 650nm incident light over a ±6° range of incident angles. The data was collected using the apparatus shown in Figure 9. Two overlapping bands are observable, a less intense band at -1.7° and a more intense, yet narrower, band at 0°. Because SRSPPs are more localized, the influence of their fields more rapidly diminishes with distance than the LRSPPs. Increasing the SPCTF gap distance (Figure 15B) lessens the resonance ability of SRSPP in the cavity and provides a way to distinguish the LRSPPs from the SRSPPs.

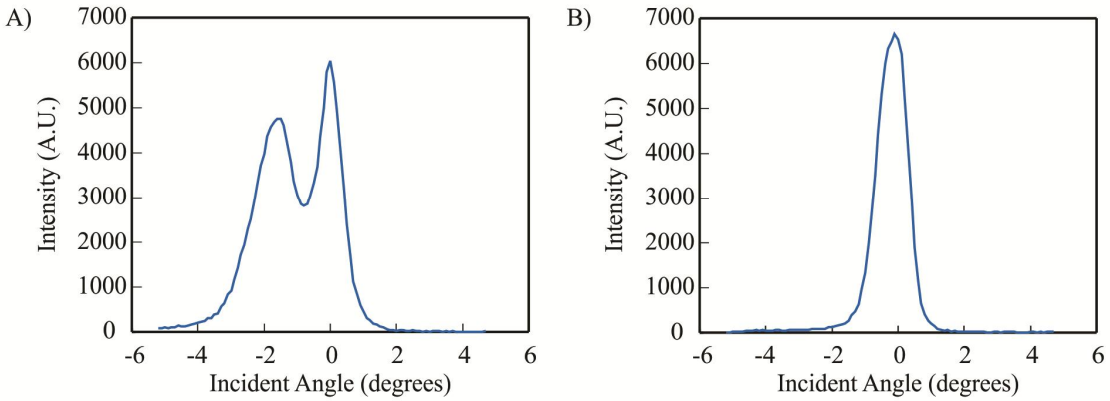

Figure 15. The dependence of SRSPPs and LRSPPs on gap distance in the SPCTF. A) Light at 650nm couples over a range of incident angles in the SPCTF. Two overlapping bands are observable and represent resonant coupling of both SRSPPs and LRSPPs. B) At a greater gap distance, only LRSPPs are able to couple with the incident light.

4.5 SPCTF acceptance angle and bandpass with angularly dispersed light.

Use of the SPCTF as a widefield filter for imaging applications requires a sufficiently large acceptance angle to permit image reformation. While apertures can be used to select those components of the Fourier space that are better collimated, doing so greatly diminishes the light intensity and reduces the signal-to-noise level. To access its potential as a widefield image filter, the SPCTF passband was studied as a function of wavelength and illumination angle using broadband angularly dispersed light (Figure 16). While the use of a grating in the optical path before a widefield tunable filter seems questionable and counterintuitive, the SPCTF is designed to be miniaturized so that it can be directly integrated with detector arrays. In some implementations, each pixel of an array detector could be integrated with its own SPCTF. Hence the SPCTF can be used to exploit the wavelength filtering superiority of (transmissive) dispersive gratings without having to rely on intensive computational methods for wavelength deconvolution.

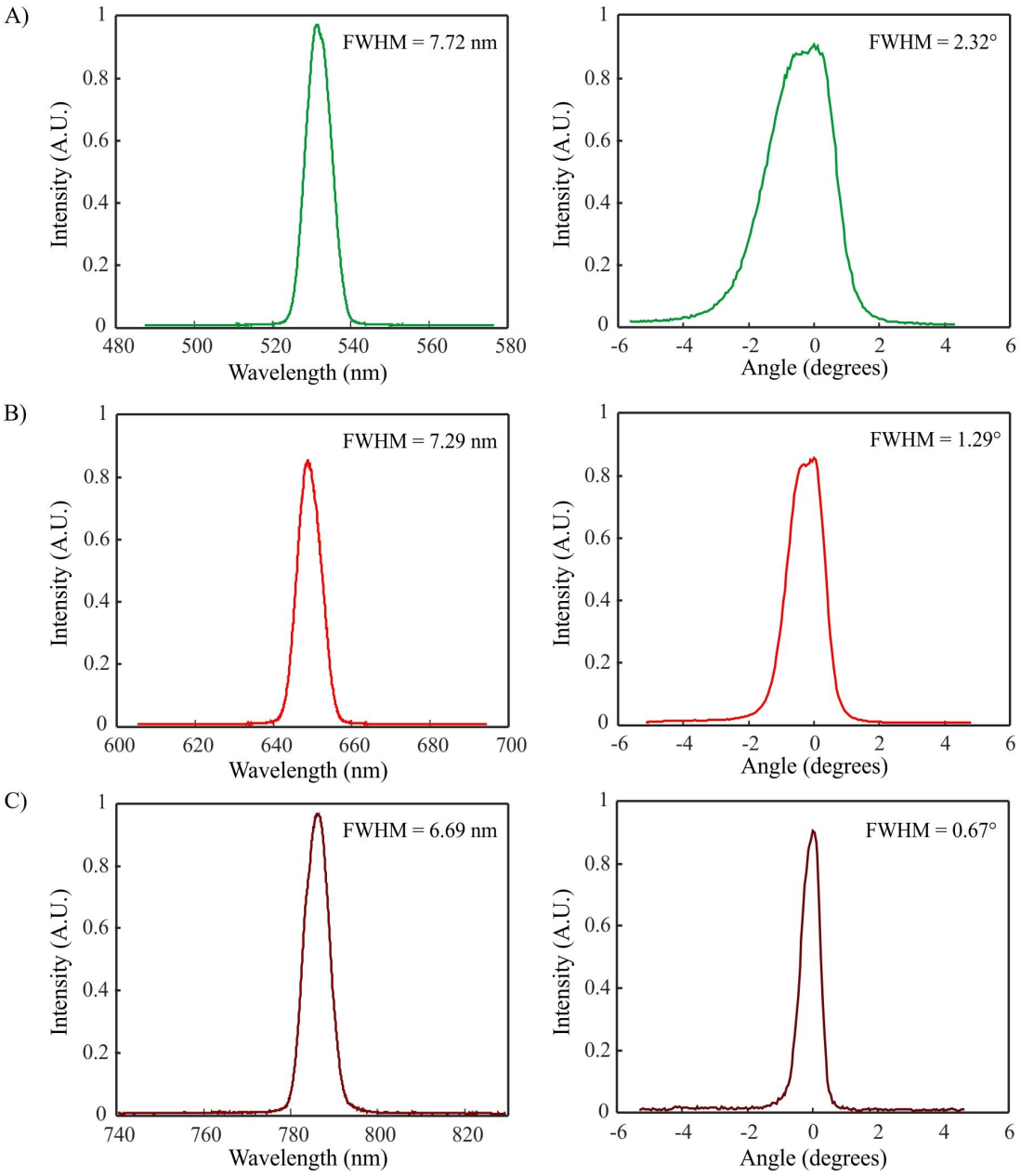

Figure 16. The bandpass and acceptance angle of the SPCTF. Spectra of the SPCTF passband are shown on the left for the A) 532nm, B) 650nm, and C) 785nm passbands. The plots on the right give the intensity of SPCTF filtered light as a function of illumination angle. The zero-angle position is selected as the angle in which the transmittance of the tuning wavelength is optimal.

4.6 SPCTF hyperspectral imaging

To explore the potential of the SPCTF for use in widefield hyperspectral imaging, a series of images were collected through the SPCTF as described in section 3.5. The collected images, shown in Figure 17, were collected at 25nm increments from 450nm to 700nm at the full pixel resolution of the CCD. Subtle wavelength-dependent changes in the intensity values between image frames are observable. A spectral identity map (SIM) was produced from the data in which shape variations in the spectra at each pixel location are exploited to generate a single pseudocolor image. Pixels

that exhibit different colors in the SIM image result correspond to differently shaped spectra in the image dataset. Because SIM is scale invariant, these color differences represent qualitative differences in composition. This data represents the first use of the SPCTF for spectral imaging.

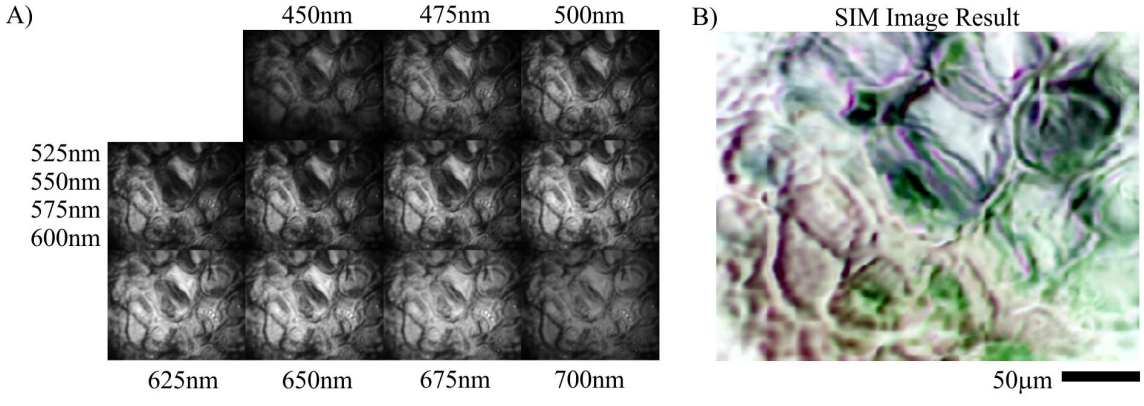

Figure 17. SPCTF spectral imaging. A) A set of widefield spectral images collected through the SPCTF as a function of passband wavelength. B) A spectral identity map (SIM) of the image data showing qualitative changes in sample composition.

5. CONCLUSIONS

A new type of tunable wavelength filter, based on surface plasmon coupling in a resonant cavity, has been introduced. The SPCTF filter is constructed from two Kretschmann-Raether metal-coated prisms. Empirical reflectance data from the glass-metal interface of the individual prism-element showed qualitative agreement with theoretical estimates. While very sensitive to the illumination angle ($<2^o$), surface plasmon generation occurs over a broad range of wavelengths and produced a nominal bandpass of ~70nm for a metal film thickness of 48nm at wavelengths between 550nm and 850nm. To exploit the angular sensitivity as a way of reducing the SPCTF bandwidth, the prism-element reflectance was measured using angularly dispersed light. Nominal bandwidths below 10nm were achieved within the spectral region between 550nm and 850nm. Without any narrowing of the passband, the two-prism SPCTF also produced a bandpass of ~70nm over the spectral range from 550nm to 850nm and exhibited a nominal percent transmittance of ~32%. The use of angularly dispersed light with the SPCTF resulted in a 10-fold narrowing of the bandpass to ~7nm (FWHM). The acceptance angle under these conditions was ~1.5^o. Lastly, proof-of-concept spectral imaging was demonstrated using the SPCTF without any dispersive element. A spectral identity map of the spectral image data confirmed wavelength dependent variability related the qualitative compositional differences.

ACKNOWLEDGEMENTS

The authors thank Nick Pallas for his help in acquiring the spectral image data and for his early work on the SPCTF, both of which helped shape our research. We are also indebted to Dr. Paul Hambourger, Associate Professor Emeritus at Cleveland State University, for conferring upon us the sputtering system he so carefully created and for his willingness to give expert help. We thank the Office of Research at Cleveland State University for partial financial support of this work through the Dissertation Research Award mechanism. We also give our appreciation to the National Science Foundation which supported portions of this work under grant No. 1126126. Any opinions, findings, and conclusions or recommendations expressed in this material are those of the authors and do not necessarily reflect the views of the National Science Foundation.

REFERENCES

[1] Calin, M. A., Parasca, S. V., and Manea, D. "Hyperspectral imaging in the medical field: present and future," *Applied Spectroscopy Reviews,* **49**(6)*,* 435-447 (2014).

[2] Pu, Y. Y., Feng Y. Z., and Sun, D. W., "Recent progress of hyperspectral imaging on quality and safety inspection of fruits and vegetables: a review," *Comprehensive Reviews in Food Science and Food Safety*, **14**(2), 176-188 (2015).

[3] Serranti, S., Gargiulo, A., and Bonifazi, G, "Classification of polyolefins from building and construction waste using NIR hyperspectral imaging system," *Resour. Conserv. Recycling,* **61**, 52-58 (2012).

[4] Palmieri, R., Bonifazi, G., and Serranti, S., "Recycling-oriented characterization of plastic frames and printed circuit boards from mobile phones by electronic and chemical imaging," *Waste Manage.,* **34**(11), 2120-2130 (2014).

[5] Arnold, G. E., "Infrared remote sensing of planetary surfaces: An overview, outstanding questions, and prospects," *Proc. SPIE* **8867**, 886703 (2013).

[6] Houle, M. A., Burruss, R. C., Ridsdale, A., Moffatt, D. J., Légaré, F., and Stolow, A., "Rapid 3D chemical-specific imaging of minerals using stimulated Raman scattering microscopy," *J. Raman Spectrosc.,***48**(5), 726-735 (2017).

[7] Scafutto, R. D. M., de Souza Filho, C. R., and Rivard, B., "Characterization of mineral substrates impregnated with crude oils using proximal infrared hyperspectral imaging," *Remote Sens. Environ.,* **179,** 116-130 (2016).

[8] Abuleil, M. and Abdulhalim, I., "Narrowband multispectral liquid crystal tunable filter," *Opt. Lett.* **41**(9)*,* 1957-1960 (2016).

[9] Zheng, J., Wang, K., Gao, H., Lu, F., Sun, L., and Zhuang, S., "Multi-wavelength sensitive holographic polymer dispersed liquid crystal grating applied within image splitter for autostereoscopic display," *SPIE Photonic Fiber and Crystal Devices: Advances in Materials and Innovations in Device Applications X,* 995818, (2016).

[10] Patel, J. S., Saifi, M. A., Berreman, D. W., Lin, C., and Andreadakis, N., "Electrically tunable optical filter for infrared wavelength using liquid crystals in a Fabry–Perot etalon," *Appl. Phys. Lett.,* **57**(17)*,* 1718-1720 (1990).

[11] Schaeberle, M. D., Morris, H. R., Turner II, J. F., and Treado, P. J., "Raman chemical imaging spectroscopy," *Anal. Chem.,* **71**(5), 175A-181A (1999).

[12] Morris, H. R., Turner II, J. F., Munro, B, Ryntz, R. A., and Treado, P. J., "Chemical imaging of thermoplastic olefin (TPO) surface architecture," *Langmuir,* **15**(8), 2961-2972 (1999).

[13] Zuzak, K. J., Schaeberle, M. D., Lewis, N. E., and Levin, I. W., "Visible reflectance hyperspectral imaging: characterization of a noninvasive, in vivo system for determining tissue perfusion," *Anal. Chem.,* **74**(9), 2021-2028 (2002).

[14] Turner II, J. F. and Treado, P. J., "LCTF Raman chemical imaging in the near infrared," *SPIE: Aerosense'97*, 280-283 (1997).

[15] Pappas, D., Matveev, O. I., Smith, B. W., Shepard. M. R., Podshivalov, A. A., and Winefordner, J. D., "Sealed-cell mercury resonance ionization imaging detector," *Appl. Opt.,* **39**(27), 4911-4917 (2000).

[16] Temirov, J. P., Chigarev, N. V., Matveev, O. I., Smith, B. W., and Winefordner, J. D., "A resonance ionization imaging detector based on cesium atomic vapor," *Spectrochimica Acta Part B: Atomic Spectroscopy,* **59**(5), 677-687 (2004).

[17] Daly, J. T., Bodkin, A., Schneller, W., Kerr, R., Noto, J., Haren, R., Eismann, M., and Karch, B., "Tunable narrow-band filter for LWIR hyperspectral imaging," *Proc. SPIE* **3948***,*104-115 (2000).

[18] Marinelli, W. J., Gittins, C. M., Gelb, A. H., and Green, B. D, "Tunable Fabry–Perot etalon-based long-wavelength infrared imaging spectroradiometer," *Appl. Opt.,* **38**(12), 2594-2604 (1999).

[19] Hufziger, K. T., Bykov, S. V. and Asher, S. A., "Raman hyperspectral imaging spectrometer utilizing crystalline colloidal array photonic crystal diffraction," *Appl. Spectrosc.,* **68**(11), 1219-1223 (2014).

[20] Hufziger, K. T., Bykov, S. V. and Asher, S. A., "Ultraviolet Raman wide-field hyperspectral imaging spectrometer for standoff trace explosive detection," *Appl. Spectrosc.,* **71**(2), 173-185 (2017).

[21] Bhargava, R., Wall, B. G., and Koenig, J. L., "Comparison of the FT-IR mapping and imaging techniques applied to polymeric systems," *Appl. Spectrosc.,* **54**(4),470-479 (2000).
[22] Turner II, J. F., and Treado, P. J., "Near-infrared acousto-optic tunable filter Hadamard transform spectroscopy," *Appl. Spectrosc.,***50**(2), 277-284 (1996).
[23] Schaeberle, M. D., Turner II, J. F., and Treado, P. J., "Multiplexed acousto-optic tunable filter (AOTF) spectral imaging microscopy," *IS&T/SPIE 1994 International Symposium on Electronic Imaging: Science and Technology,* 11-20 (1994).
[24] Storey, A. P., Ray, S. J., Hoffmann, V., Engelhard, C., Buscher, W., and Hieftj, G. M., "Wavelength scanning with a tilting interference filter for glow-discharge elemental imaging," *Appl. Spectrosc.,* **71**(6), 1280-1288 (2017).
[25] Gowen, A. A., O'Donnell, C. P., Cullen, P. J., and Bell, E. J., "Recent applications of chemical imaging to pharmaceutical process monitoring and quality control," *European Journal of Pharmaceutics and Biopharmaceutics,* **69**(1),10-22 (2008).
[26] Piqueras, S., Duponchel, L., Tauler, R., and de Juan, A., "Monitoring polymorphic transformations by using in situ Raman hyperspectral imaging and image multiset analysis," *Anal. Chim. Acta,* **819**, 15-25 (2014).
[27] Wold, J. P. "On-line and non-destructive measurement of core temperature in heat treated fish cakes by NIR hyperspectral imaging," *Innovative Food Science & Emerging Technologies,* **33**, 431-437 (2016).
[28] Manolakis, D. G., Golowich, S. E., and DiPietro, R. S., "Long-wave infrared hyperspectral remote sensing of chemical clouds: A focus on signal processing approaches," *IEEE Signal Process. Mag.,* **31**(4), 120-141 (2014).
[29] Cucci, C., Delaney, J. K., and Picollo, M., "Reflectance hyperspectral imaging for investigation of works of art: old master paintings and illuminated manuscripts," *Acc. Chem. Res.,***49**(10), 2070-2079 (2016).
[30] Morampudi, R., "Development of a high resolution wavelength filter and a spatially multiplexed raman imaging system," Cleveland State University, Cleveland, OH, USA (2014).
[31] Deverse, R. A., "Multiplexed hyperspectral imaging and spectrometry using spatial light modulators", Kansas State University, Manhattan, KS, USA, (1999).
[32] Schlücker, S., Schaeberle, M. D., Huffman, S. W., and Levin, I. W., "Raman microspectroscopy: a comparison of point, line, and wide-field imaging methodologies," *Anal. Chem.,* **75**(16), 4312-4318 (2003).
[33] Sun, B., Edgar, M. P., Bowman, R., Vittert, L. E., Welsh, S., Bowman, A., and Padgett, M. J., "3D computational imaging with single-pixel detectors," *Science,* **340**(6134), 844-847 (2013).
[34] Nash, D. J. and Sambles, J. R., "Surface plasmon-polariton study of the optical dielectric function of silver," *Journal of Modern Optics*, **43**(1), 81-91 (1996).
[35] Kretschmann, E., "Die bestimmung optischer konstanten von metallen durch anregung von oberflächenplasmaschwingungen," *Zeitschrift für Physik* **241**(4), 313-324 (1971).
[36] de Bruijn, H. E., Kooyman, R. P. H., and Greve, J., "Determination of dielectric permittivity and thickness of a metal layer from a surface plasmon resonance experiment," *Appl. Opt.,* **29**(13), 1974-1978 (1990).
[37] Berini, P., "Long-range surface plasmon polaritons", *Advances in Optics and Photonics* **1**(3), 484–588 (2009).
[38] Turner II, J. F., Zhang, J., and O'Connor, A., "A spectral identity mapper for chemical image analysis," *Appl. Spectrosc.,* **58**(11), 1308-1317 (2004).